PHYSICAL REVIEW B **86**, 024420 (2012)

Strain-driven transition from E-type to A-type magnetic order in $YMnO_3$ epitaxial films

F. Jiménez-Villacorta,[1] J. A. Gallastegui,[2] I. Fina,[3] X. Marti,[4,*] and J. Fontcuberta[3]
[1]*Department of Chemical Engineering, Northeastern University, Boston, Massachusetts 02115, USA*
[2]*SpLine Spanish CRG Beamline at the European Synchrotron Radiation Facility, ESRF BP 220-38043 Grenoble Cedex, France and Instituto de Ciencia de Materiales de Madrid (ICMM-CSIC) Cantoblanco E-28049 Madrid, Spain*
[3]*Institut de Ciència de Materials de Barcelona (ICMAB-CSIC), Campus UAB, 08193 Bellaterra, Spain*
[4]*Charles University in Prague, Faculty of Mathematics and Physics, Prague, Czech Republic*
(Received 7 February 2012; revised manuscript received 3 May 2012; published 16 July 2012)

Single-crystal (100)-oriented $YMnO_3$ thin films grown on (110)-oriented $SrTiO_3$ substrates have been studied by polarized extended x-ray absorption fine structure to determine the Mn-O bond lengths. Using a simple geometrical model and previously reported x-ray diffraction data on the same samples, the Mn-O-Mn bonding angles are calculated. We show that the epitaxy-induced in-plane anisotropic strain has a dramatic impact on the bonding angles, allowing the rationalization of the reported existence of cycloidal magnetic order and concomitant ferroelectricity in moderately strained films and the gradual suppression by larger strains. We shall argue that epitaxial strain allows shifting $YMnO_3$ from an E-type to A-type antiferromagnetic ground state, crossing a cycloidal magnetic region.

DOI: 10.1103/PhysRevB.86.024420 PACS number(s): 75.70.−i, 61.05.cj, 75.85.+t, 77.55.Nv

Orthorhombic $RMnO_3$ (R = Y, Sm-Lu) oxides have fueled extensive research efforts because the ferroelectric properties, stemming from the antiferromagnetic ordering, point to an inherent strong coupling between both ferroic orders.[1] Whereas for R = Y and the smaller rare-earth elements (R = Ho-Lu), bulk $RMnO_3$ oxides are found to have a collinear antiferromagnetic ordering.[2,3] The reported ferroelectric properties of $YMnO_3$ thin films indicate the occurrence of a cycloidal ordering[4] or the coexistence of cycloidal and E-type antiferromagnetic orderings.[5,6] Since the Mn-O-Mn bonding angle [Fig. 1(a)] is the fundamental parameter determining the magnetic ground structure in the bulk $RMnO_3$ phase diagram,[7] and therein bulk $YMnO_3$ lies at the verge between cycloidal and E-type order, it is tempting to speculate that epitaxial strain could modify the bonding angles in the required way to conciliate the observed transition from E-type into cycloidal magnetic ordering.[4,8] However, from this point of view, not only the observation that ferroelectricity but also its suppression in more strained $YMnO_3$ films[4,8] is intriguing and illustrates that more information is required to achieve a solid understanding of the role of strain on the magnetic phase diagram of $RMnO_3$ oxide thin films.

In this paper, we address the experimental measurement of the Mn-O-Mn bonding angle in orthorhombic $YMnO_3$ thin films. We combine x-ray diffraction (XRD) and polarized x-ray absorption fine structure (EXAFS) experiments to quantify the bonding angle and its trend with increasing substrate-induced epitaxial strain. We conclude that by reducing the film thickness, the increased epitaxial strain leads to an increasing bonding angle that pushes the antiferromagnetic ground state from the bulk E-type toward the A-type across the region of cycloidal order. Our findings are in agreement with the experimental observation of cycloidal order in $(100)YMnO_3/(110)SrTiO_3$ samples and a gradually reduced polarization, while decreasing the film thickness.[4,8]

In the case of bulk single crystals or powder samples of $RMnO_3$, the bonding angle θ [Fig. 1(a)] can be easily determined by diffraction techniques (neutron or x-ray). In addition, to monitor lattice distortions, experiments under hydrostatic pressure[9,10] or chemical substitution[11] have been attempted. Distinct variations of the bonding angles have been reported: an increase of the bonding angle θ upon compressing the unit cell volume[9,10] or a decrease of θ by reducing unit cell volume by appropriate chemical substitution at the Y site in $YMnO_3$.[11] These results anticipate a complex structural response of $YMnO_3$ thin films even when grown on cubic single-crystalline substrates; indeed, it has been shown than the resulting in-plane strain is anisotropic,[12] and thus it cannot be compared to any bulk experiment. Understanding the magnetic order and the multiferroic properties of $RMnO_3$ thin films requires the determination of the bonding angle θ and its variation upon changing the strain state. Moreover, in the case of thin films, the routinely available XRD experiments are well suited to extract unit cell distances but are rather inappropriate to determine the required bonding angle θ, thus emphasizing the need for alternative tools.

For this experiment we selected two $(100)YMnO_3$ films having remarkably different dielectric properties and lattice parameters. The $(100)YMnO_3$ films of two different thicknesses ($t = 106$ and 49 nm) were grown on single-crystalline $(110)SrTiO_3$ substrates. Details on x-ray characterization and ferroelectric properties of the very same films can be found elsewhere.[4,8] Of relevance here is that both films are found to be single domain and (100) textured. The measured cell parameters (a,b, and c) are (5.260, 5.712, and 7.453 Å) and (5.260, 5.700, and 7.430 Å) for $t = 106$ nm and $t = 49$ nm, respectively. Values are summarized in Table I.

Our approach to evaluate the bonding angle θ is illustrated in Fig. 1(a). On the one hand, from XRD we obtain the lattice parameters and the distance $d = \sqrt{[(a/2)^2 + (b/2)^2]}$ [Fig. 1(a)]. On the other hand, EXAFS data have been used to determine the bonding distances L and S. The bonding angle can be subsequently determined by using

$$\theta = arccos\,[(\mathrm{L}^2 + \mathrm{S}^2 - d^2)/(2\mathrm{LS})]. \qquad (1)$$

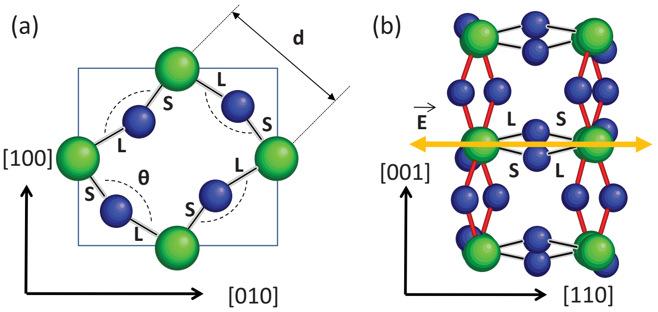

FIG. 1. (Color online) (a) Sketch of a Mn oxide (001) plane in orthorhombic $YMnO_3$ (Pbnm setting). Manganese and oxygen atoms are depicted in green (larger) and blue (smaller), respectively. Notice the alternating sequence of short (S) and long (L) Mn-O bonds occurring in the (001) plane. While the distance between Mn atoms (d) is obtained by XRD, the Mn-O bond lengths (L and S) are obtained by EXAFS. Finally, the bonding angle θ is calculated using the cosine law.

X-ray absorption spectroscopy measurements in the fluorescence yield mode at the Mn K-edge were performed in the Spanish Collaborating Research Group (CRG) beamline (SpLine-BM25A) of the European Synchrotron Radiation Facility (ESRF). The sample was mounted so the incoming linearly polarized x-ray beam has the polarization vector along [110; thick arrow in Fig. 1(b)]; within this configuration EXAFS exclusively probes the basal contributions associated with the nearest neighbors at long and short distances [L and S, respectively, see Fig. 1(b)]. The incident beam was monitored using a N_2-filled gas ionization chamber, and Mn K_α fluorescence lines were collected using a 13-element Si(Li) detector. Each EXAFS-collected curve consisted of several spectra to improve the signal-to-noise ratio with data acquired up to $k_{\max} = 14\,\text{Å}^{-1}$. Data treatment was performed using the ATHENA software[13] and the EXAFS analysis was performed using the VIPER package.[14]

Raw EXAFS spectra [Fig. 2(a), symbols] were weighted using a Hanning window in the Fourier transform centered at the first coordination sphere for Mn (∼1–2 Å) in order to preserve the contributions of L and S and disregarding all other distances not relevant for the present study [Fig. 2(a), dashed line], as typically employed in EXAFS analysis (see, for instance, Refs. 15–17). Amplitude and phase functions models for Mn-O bond lengths were obtained with the FEFF8 code[18] and iterated until obtaining the satisfactory simultaneous fit of both the filtered EXAFS oscillations [Fig. 2(a), solid line] and their Fourier transforms [Fig. 2(b), solid line]. It can be appreciated in Fig. 2(b) that for both films, at ∼1.5 Å, a pronounced peak with a well-defined shoulder ∼2 Å is clearly visible that likely corresponds to the L and S bond lengths. Because we expect L and S to be rather similar and the resolution of EXAFS is estimated to be about $\Delta r = \pi/2\Delta k \approx 0.14\,\text{Å}$, the corresponding Fourier transform of the radial distribution function shall manifest as strongly overlapping rather than isolated peaks as observed in Fig. 2(b). From the fits, two distinguishable contributions, attributed to the L and S bond lengths, are extracted for each film and shown in Table I.

To estimate the error bars in the determination of the bond lengths, the quality of the Fourier-filtered EXAFS oscillation fit as a function of the two parameters (bond lengths L and S), was assessed by computing the (normalized) sum of residuals (R)

$$R = \frac{\sum_n k_n^2 |\chi_{\text{exp}}(k_n) - \chi_{\text{fit}}(k_n)|}{\sum_n k_n^2 |\chi_{\text{exp}}(k_n)|} \times 100, \tag{2}$$

where $k^2\chi_{\text{exp}}$ is the experimental EXAFS signal filtered to the first coordination sphere. The lowest values of R cover a range that coincides with the precision in neighbor distances determined by EXAFS, typically ±0.01 Å. R-factor maps as a function of S and L have been made for each film as shown in Figs. 2(c) and 2(d). Inspection of these R maps indicates that the minima of R(L,S) are well defined, and thus L and S can be safely determined for each film. It is clear that for the thinnest YMO film (49 nm), both L and S are shorter than for the thicker film, thus illustrating the enhanced strain state of the former. Using the corresponding (L,S) values, the Mn-O-Mn basal bonding angle θ (calculated with the mentioned geometric relation) can be evaluated. It turns out that θ increase, i.e., the bond opens, while decreasing the film thickness.

From data summarized in Table I, it follows that the bonding angle θ for the thickest film (less strained) is ∼147°, which is closer to that reported for bulk $TbMnO_3$ and significantly larger than that of bulk $YMnO_3$. When reducing film thickness, the bonding angle θ increases up to $\theta = 149.4^\circ$, thus approaching $\theta \approx 150^\circ$, as reported for $NdMnO_3$. This variation of bonding angles suggests that for the thicker $YMnO_3$ film, a cycloidal magnetic structure, as in $TbMnO_3$, should be expected, whereas for the thinner, and more strained

TABLE I. Calculated long (L) and short (S) bond-lengths from the EXAFS experiments, Mn-Mn distances (d) measured in Ref. 8 from XRD and the calculated Mn-O-Mn bonding angle (θ). The magnetic structure in each case is indicated in the last column. Asterisks denote the bulk values obtained from the literature (Ref. 11).

Sample	S (Å) ±0.01 Å	L (Å) ±0.01 Å	d (Å) ±0.005 Å	θ (°) ±1.5 °	Magnetic structure
Thin film 106 nm	1.91	2.14	3.88	146.8	Cycloidal[4,8]
Thin film 49 nm	1.90	2.12	3.88	149.4	Cycloidal + A-type[4,8]
Bulk $YMnO_3$	1.90*	2.20*	3.91*	144.5*	E-type[2,3,7]
Bulk $TbMnO_3$	1.91*	2.21*	3.94*	145.4*	Cycloidal[7,19]
Bulk $NdMnO_3$	1.91*	2.21*	3.97*	150.0*	A-type[7,11]

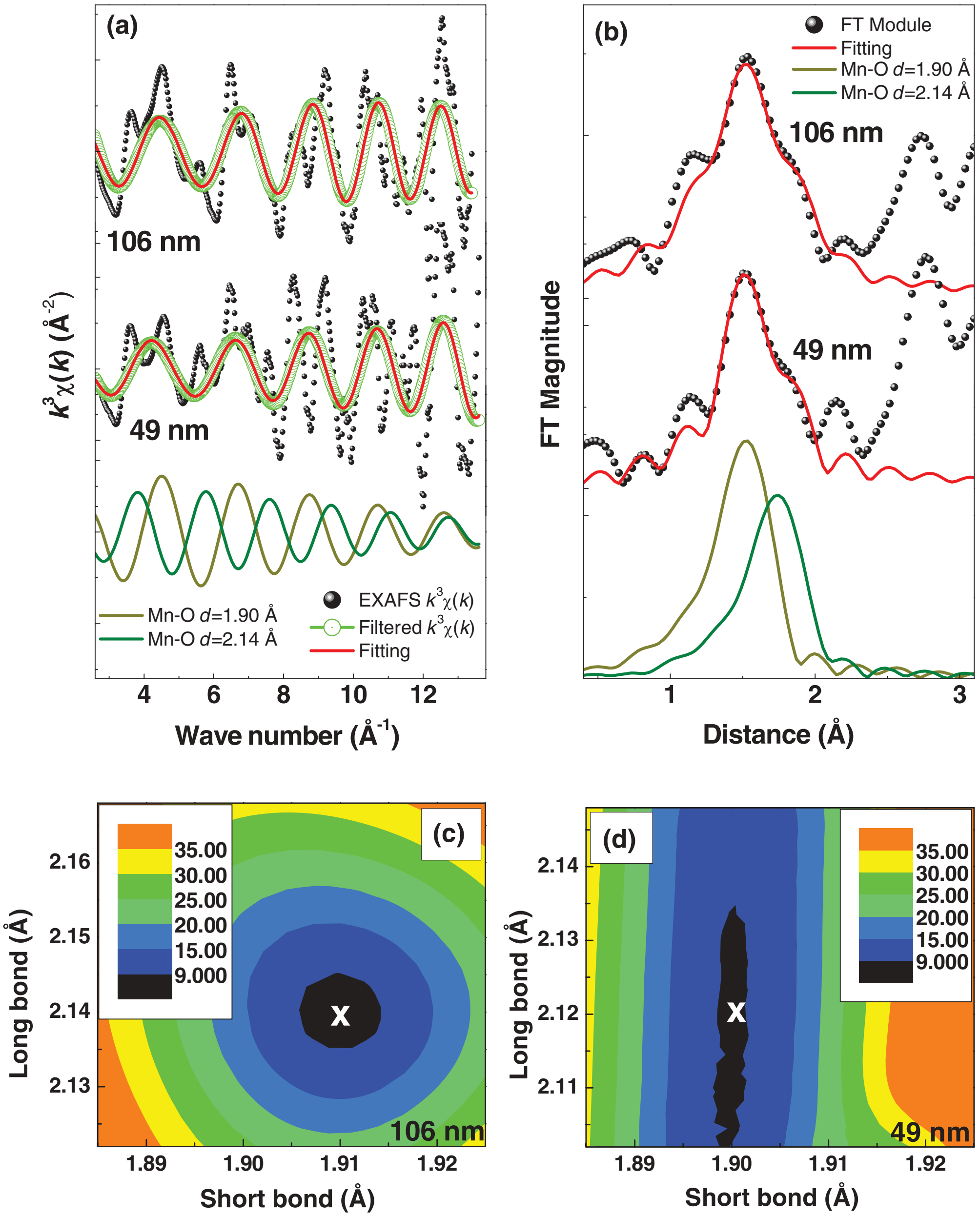

FIG. 2. (Color online) (a) Raw experimental EXAFS signals (symbols), the filtered signals (dashed lines), and the corresponding fit (solid line) for the two studied samples. Theoretically modeled curves for a single bond-length contribution are shown below for two indicated distances. (b) Fourier transform modulus (circles) and fitting (solid lines) from the EXAFS signals shown in panel (a). (c) and (d) *R* factor as a function of long bond and short bond distances for the films with 106 nm and 49 nm thickness, respectively. *R* factor shown in the legend measures the goodness of the fits (the lower *R* factor the better fit).

film, a magnetic structure approaching the *A*-type phase, as in $NdMnO_3$, should be anticipated. This trend is in agreement with magnetic and dielectric data reported in Refs. 4 and 8. To illustrate the trends, the results for thin films have been plot in an L-S map (Fig. 3), also including the bulk L-S values. The color scale corresponds to the bonding angle calculated from Eq. (1), assuming $d = 3.88$ Å, which is similar for both studied samples despite the notable differences in lattice parameters and dielectric properties. Solid black lines correspond to the bulk magnetic phase boundaries according to the bonding angles.[7]

The position of the bulk $YMnO_3$ evidences that the strain-induced distortion opens the bonding angle and pushes the magnetic structure away from the *E*-type (bulk $YMnO_3$), well into the *A*-type (here reported $YMnO_3$ 49-nm film), crossing the cycloidal region (here reported $YMnO_3$ 106-nm film). Therefore, we highlight that the displayed data suggest that the epitaxial strain determines the magnetic ordering through the modification of structural topology, with the bonding angle being the key parameter.

In summary, we have measured the short (S) and long (L) bond lengths using EXAFS in differently strained, epitaxial

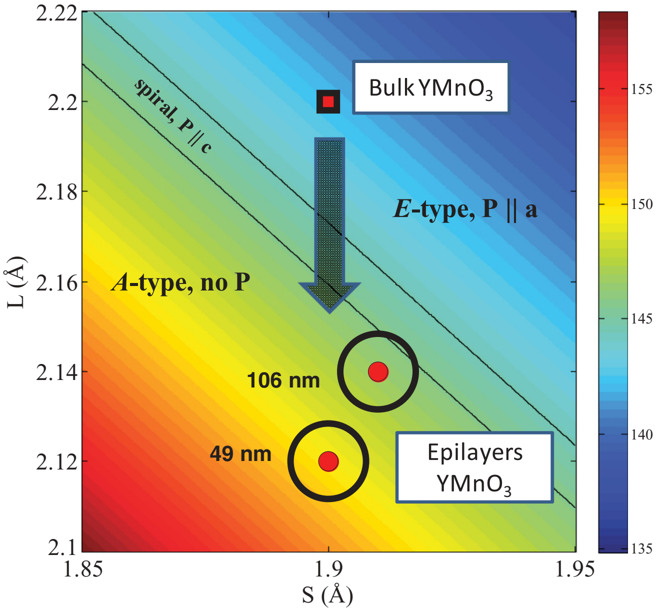

FIG. 3. (Color online) Trend of the L and S distances in epitaxial YMnO$_3$ thin films grown on (110)SrTiO$_3$ substrates. The 106- and 49-nm-thick samples are depicted with circles. Circumference around the circles corresponds to the experimental uncertainty. Square symbol denotes the L and S values for bulk YMnO$_3$ (from Ref. 11). The color scale indicates the bonding angle calculated from Eq. (1) and using a fixed $d = 3.88$ Å, similar for both samples (Table I). The solid lines denote the bonding angle phase boundaries in bulk RMnO$_3$ compounds of the E-type, cycloidal, and A-type magnetic orderings according to Ref. 7.

(100)YMnO$_3$ thin films. Combining these values with previously reported X-ray diffraction data, we have computed the Mn-O-Mn superexchange angle θ. Our experiments demonstrate that the bonding angle gradually opens under the in-plane anisotropic strain imposed by the (110)SrTiO$_3$ substrates. We suggest that this variation of the bonding angle determines a gradual change of the antiferromagnetic order, from cycloidal to A-type, which nicely matches the existing phase diagram for bulk RMnO$_3$ manganites and provides a robust structural basis to understand their multiferroic properties. We expect that the methodology employed here to determine the critical bonding angle, which combines diffraction and absorption x-ray data, would be useful in many other cases in which bonding angles and distances in thin films were of interest.

ACKNOWLEDGMENTS

We thank the SpLine staff for their assistance in using Spanish CRG beamline (BM25A-SpLine) at ESRF, the Spanish Ministry of Science for the beam-time allocation and experiment funding, and D. Pesquera and F. Sánchez for their contributions during measurements and skills on sample preparation. The financial support of the Spanish Ministerio de Ciencia e Innovación (MAT2011-29269-CO3-01 and CSD2007-00041), Consejo Superior de Investigaciones Científicas (funding of the ESRF experiment and Project No. CSIC PI201060E013), Generalitat de Catalunya (2009 SGR-376) EU, and the Grant Agency of the Czech Republic No. P204/11/P339 is also acknowledged.

---

[*] Corresponding author: xaviermarti@berkeley.edu; now at Department of Materials Science and Engineering, University of California, Berkeley, USA.

[1] T. Kimura, T. Goto, H. Shintani, K. Ishizaka, T. Arima, and Y. Tokura, Nature (London) **426**, 55 (2003).

[2] A. Muñoz, J. A. Alonso, M. T. Casais, M. J. Martínez-Lope, J. L. Martínez, and M. T. Fernández-Díaz, J. Phys.: Condens. Matter **14**, 3285 (2002).

[3] D. Okuyama, S. Ishiwata, Y. Takahashi, K. Yamauchi, S. Picozzi, K. Sugimoto, H. Sakai, M. Takata, R. Shimano, Y. Taguchi, T. Arima, and Y. Tokura, Phys. Rev. B **84**, 054440 (2011).

[4] I. Fina, L. Fàbrega, X. Martí, F. Sánchez, and J. Fontcuberta, Appl. Phys. Lett. **97**, 232905 (2010).

[5] M. Nakamura, Y. Tokunaga, M. Kawasaki, and Y. Tokura, Appl. Phys. Lett. **98**, 082902 (2011).

[6] H. Wadati, J. Okamoto, M. Garganourakis, V. Scagnoli, U. Staub, Y. Yamasaki, H. Nakao, Y. Murakami, M. Mochizuki, M. Nakamura, M. Kawasaki, and Y. Tokura, Phys. Rev. Lett. **108**, 047203 (2012).

[7] T. Goto, T. Kimura, G. Lawes, A. P. Ramirez, and Y. Tokura, Phys. Rev. Lett. **92**, 257201 (2004).

[8] J. Fontcuberta, I. Fina, L. Fàbrega, F. Sánchez, X. Martí, and V. Skumryev, Phase Transitions **84**, 555 (2010).

[9] J. M. Chen, T. L. Chou, J. M. Lee, S. A. Chen, T. S. Chan, T. H. Chen, K. T. Lu, W. T. Chuang, H.-S. Sheu, S. W. Chen, C. M. Lin, N. Hiraoka, H. Ishii, K. D. Tsuei, and T. J. Yang, Phys. Rev. B **79**, 165110 (2009).

[10] A. Y. Ramos, H. C. N. Tolentino, N. M. Souza-Neto, J.-P. Itie, L. Morales, and A. Caneiro, Phys. Rev. B **75**, 052103 (2007).

[11] J. A. Alonso, M. J. Martinez-Lope, M. T. Casais, and M. T. Fernandez-Diaz, Inorg. Chem. **39**, 917 (2000).

[12] X. Marti, F. Sanchez, V. Skumryev, V. Laukhin, C. Ferrater, M. V. Garcia-Cuenca, M. Varela, and J. Fontcuberta, Thin Solid Films **516**, 4899 (2008).

[13] B. Ravel and M. Newville, J. Synchrotron Radiat. **12**, 537 (2005).

[14] K. V. Klementiev, J. Phys. D **34**, 209 (2001).

[15] D. C. Koninsberger and R. Prins, *X-Ray Absorption: Principles, Applications, Techniques of EXAFS, SEXAFS and XANES* (Wiley, New York, 1988).

[16] F. Jiménez-Villacorta, E. Céspedes, M. Vila, A. Muñoz-Martín, G. R. Castro, and C. Prieto, J. Phys. D **41**, 205009 (2008).

[17] F. Jiménez-Villacorta, A. Muñoz-Martín, and C. Prieto, J. Appl. Phys. **96**, 6224 (2004).

[18] A. L. Ankudinov, B. Ravel, J. J. Rehr, and S. D. Conradson, Phys. Rev. B **58**, 7565 (1998).

[19] M. Kenzelmann, A. B. Harris, S. Jonas, C. Broholm, J. Schefer, S. B. Kim, C. L. Zhang, S. W. Cheong, O. P. Vajk, and J. W. Lynn, Phys. Rev. Lett. **95**, 087206 (2005).